ELSEVIER

Journal of Fluids and Structures 24 (2008) 449–466

JOURNAL OF FLUIDS AND STRUCTURES

www.elsevier.com/locate/jfs

Flow-induced motion of a short circular cylinder spanning a rectangular channel

M. Lazarkov, J. Revstedt*

Energy Sciences/Fluid Mechanics, LTH, Lund University, P.O. Box 118, S-221 00 Lund, Sweden

Received 16 March 2006; accepted 7 October 2007
Available online 3 December 2007

Abstract

Flow-induced oscillation of an elastically supported circular cylinder subject to an incompressible fluid at $Re = 100$ and 400 has been studied using three-dimensional simulations. The cylinder is either subjected to a uniform flow in an unconfined surrounding or confined by rectangular channel, i.e. the cylinder is confined in both the span-wise and the cross-stream directions. The cylinder surface is represented by a virtual boundary method which replaces a solid object in flow by additional force distribution to satisfy local boundary condition. The simulations have been performed for nondamped cylinder with low mass ratio. For the unconfined cylinder, the effects of Reynolds number are studied. The effects of confinement have been investigated by varying the extent of the channel (and thereby also the cylinder length) in the span-wise direction. The maximal amplitude is found to be decreased by the confinement. For very strong confinement (short cylinder) the motion of the cylinder is governed by the natural frequency of the structure even beyond synchronisation range. The upper boundary of the synchronisation range exhibits no dependency on the confinement, only on Reynolds number.
© 2007 Elsevier Ltd. All rights reserved.

Keywords: Flow-induced motion; Virtual boundary method; Cartesian grid; Moving boundaries

1. Introduction

The interaction of the flow with solid structures is a central problem in many industrial applications, e.g. flow in gas turbines around blades and foils, air motion around cables and chimneys, water motion around offshore riser pipes etc. Reviews on flow-induced vibration of structures have been published by Parkinson (1989), Bearman (1984) and Sarpkaya (1979). One of this class of problem is the canonical problem of the flow-induced vibration of an elastically constrained three-dimensional circular cylinder. The vibration is permitted only transverse to the free-stream. The system is described by the following structural parameters: mass m (associated density ρ_b), damping b, spring constant k and cylinder diameter D. The fluid parameters are the fluid density ρ, kinematic viscosity v and free-stream velocity U_∞. One of the important notions related with oscillating structures is a natural or mechanical frequency of the structure $\omega_N = \sqrt{k/m}$. The equation of motion of the cylindrical structure, determined by the structural parameters m,

*Corresponding author. Tel.: +46 46 222 4302; fax: +46 46 222 4717.
E-mail address: johan.revstedt@vok.lth.se (J. Revstedt).

0889-9746/$ - see front matter © 2007 Elsevier Ltd. All rights reserved.
doi:10.1016/j.jfluidstructs.2007.10.003

b and k, is

$$m\frac{\mathrm{d}^2x}{\mathrm{d}t^2}+b\frac{\mathrm{d}x}{\mathrm{d}t}+kx=F_x, \tag{1}$$

where F_x is the instantaneous lift force and x is the transverse displacement.

In practice, Eq. (1) usually is recast into a nondimensional form. In the literature several ways of nondimensionalisation (and, respectively, several sets of nondimensional parameters) are used. Traditionally, nondimensionalisation is performed by introducing the structural quantities

$$x^*=\frac{x}{D},\quad t^*=t\omega_N,\ \ \zeta=\frac{b}{2\sqrt{km}},\ \ U^*=\frac{U_\infty}{\omega_N D}, \tag{2}$$

which leads to the following form of Eq. (1):

$$\frac{\mathrm{d}^2x^*}{\mathrm{d}t^{*2}}+2\zeta\frac{\mathrm{d}x^*}{\mathrm{d}t^*}+x^*=C_x n U^{*2}, \tag{3}$$

where $C_x=2F_x/(\rho U_\infty^2 DL)$ is a transverse force coefficient and $n=\rho D^2L/(2m)$ is a mass parameter. The structural parameters defining the behaviour of the system in this case are ζ, n and U^*. As one can see, $\omega_N=2\pi f_N$ is used in scaling of time and velocity, producing the so-called ''reduced velocity'' U^*. However, in the situation when $m=0$ or $k=0$, the damping ζ or the natural frequency f_N can be infinite and this may lead to certain difficulties. To avoid this, another set of nondimensional parameters, based on scaling with flow variables rather than the mechanical ones, have been introduced by Shiels et al. (2001), namely

$$x^*=\frac{x}{D},\quad t^*=t\frac{U_\infty}{D},\ \ \mu^*=\frac{2\mu}{\rho D^2}=\frac{\pi\rho_b}{2\rho},\ \ \beta^*=\frac{2\beta}{\rho U_\infty D},\ \ \kappa^*=\frac{2\kappa}{\rho U_\infty^2}, \tag{4}$$

where μ, β and κ are the mass, damping coefficient and elasticity coefficient per unit span, respectively. This leads to the following form of Eq. (1):

$$\mu^*\ddot{x}^*+\beta^*\dot{x}^*+\kappa^*x^*=C_x(t^*). \tag{5}$$

Here all derivatives are taken with respect to t^*, C_x is the usual nondimensional transverse force per unit span, exerted on the body by the flow. In this case, the structure motion is determined by the nondimensional mass μ^*, damping β^* and stiffness κ^*.

Studies of flow-induced vibration of different structures have often been focused on finding the conditions (or combinations of flow and structural parameters) which may lead to high amplitude vibration of the structure. Often this occurs in the resonance case when the vortex shedding frequency f_s is close to natural frequency f_N (so-called ''lock-in'') (Feng, 1968; Koopmann, 1967). When the cylinder oscillation frequency f is synchronised with the shedding wake frequency, a good approximation of the force $F_x(t)$ and the cylinder displacement $x(t)$ in Eq. (1) is

$$F_x(t)=F_0\sin(\omega t+\phi),\quad x(t)=A\sin(\omega t), \tag{6}$$

where $\omega=2\pi f$, ϕ is the phase angle between the fluid force and the cylinder displacement, F_0 and A are the force and cylinder displacement oscillation amplitudes, respectively. The cylinder response in the synchronisation range can be approximated by Eq. (6). This leads to some conclusions about the unique structural parameters defining the maximal amplitude of vibration. Khalak and Williamson (1999) obtained a solution for the response amplitude and frequency directly from Eqs. (1) and (6).

In the case of high $m^*\zeta$ (where m^* is the ratio between the mass of the structure and the mass of the displaced fluid) the amplitude response has two branches—''initial'' and ''lower''—separated by a discontinuous mode transition. When $m^*\zeta$ is low, one more branch—'' the upper branch''—appears, corresponding to the higher response amplitude. In this situation two modes of transition exist. The case of low $m^*\zeta$, the two mode transitions, the relationship with the forces, wake vortex dynamics and wake velocity fields were studied by Govardhan and Williamson (2000, 2001).

Considering the case of low $m^*\zeta$, it has been found that the ''initial'' branch corresponds to the 2S mode of the wake, and ''lower'' and ''upper' branches are associated with the 2P wake mode. Here 2S mode is the mode when two single vortices are shed per cylinder oscillation cycle, and 2P is the mode when two pairs of vortices are formed per cycle. Both modes have been observed by Brika and Laneville (1993) for the case of high values of the mass ratio.

The numerical study of fluid–structure interaction for objects of complex geometry involves some computational issues. While flow around a single moving solid boundary in an infinite surrounding can be satisfactory represented using a stationary body-fitted mesh, flows considering multiple objects or the presence of solid walls will require special attention. Possible approaches include sliding or overlapping grids. However, these might lead to loss of accuracy and

longer computational times. A possibility to avoid complex mesh structures and to be able to describe several objects (deforming or nondeforming) moving relative to each other is to use a Virtual Boundary (VB) method, [e.g. Peskin (1977), Shyy et al. (1998), Esmaeeli and Tryggvason (1998)]. This paper presents the results of numerical study of vortex-induced vibration of elastically supported circular cylinders, confined in a rectangular channel, by using a VB method. The purposes of this work are to investigate the effects of confinement on the cylinder motion and to study the ability of VB method to handle fluid-solid structure interaction problems as well as the possibilities for further development of this approach to be applied to aeroelasticity tasks.

2. Mathematical and numerical formulation

2.1. Governing equations

The time-dependent, three-dimensional equations governing isothermal, incompressible flow of a Newtonian fluid can, in dimensionless form, be written as

$$\frac{\partial u_i^*}{\partial x_i^*} = 0, \tag{7}$$

$$\frac{\partial u_i^*}{\partial t^*} + u_j^* \frac{\partial u_i^*}{\partial x_j^*} = -\frac{\partial p^*}{\partial x_i^*} + \frac{1}{\mathrm{Re}} \frac{\partial}{\partial x_j^*} \frac{\partial u_i^*}{\partial x_j^*}. \tag{8}$$

These equations are made nondimensional using the cylinder diameter and the inflow velocity as reference:

$$x^* = \frac{x}{D}, \quad t^* = t\frac{U_\infty}{D}, \quad u_i^* = \frac{u_i}{U_\infty}, \quad p^* = \frac{p - p_0}{\rho U_\infty^2}. \tag{9}$$

For the system of Eqs. (7)–(8) the values of velocity should be imposed on all boundaries. At the inlet one can use a predefined velocity profile, and in the outlet a velocity or velocity gradient. At other boundaries different velocity boundary conditions may be used: no-slip—for solid walls, slip and periodical boundary conditions—for unconfined domain. Due to the usage of a staggered grid, no boundary condition for pressure is needed. Instead, the global mass conservation requirement is introduced.

In addition to the governing equations of the fluid motion (7) and (8), the cylinder motion equation should be solved at every time step. In our calculations we used the nondimensionalisation procedure which is similar to the one used by Shiels et al. (2001). However, our cylinder is short therefore we scale the structural parameters with the full cylinder length, instead of formulating the equation per unit span:

$$x^* = \frac{x}{D}, \quad t^* = t\frac{U_\infty}{D}, \quad m^* = \frac{2m}{\rho D^2 L}, \quad b^* = \frac{2b}{\rho U_\infty D L}, \quad k^* = \frac{2k}{\rho U_\infty^2 L}, \tag{10}$$

which leads to a similar form of dimensionless equation (5),

$$m^*\ddot{x}^* + b^*\dot{x}^* + k^*x^* = C_x(t), \tag{11}$$

where the lift coefficient is defined in the classical way: $C_x(t) = 2F_x(t)/(\rho U_\infty^2 DL)$. In this case the natural frequency and the reduced velocity can be written as $\omega_N = \sqrt{k/m} = \sqrt{k^*/m^*}U_\infty/D$ and $U^* = U_\infty/(\omega_N D) = 1/\omega_N^*$, respectively. The cylinder structure is assumed to be undamped, i.e. $b^* = 0$.

2.2. Flow solver

The system of incompressible Navier–Stokes equations (7) and (8) is discretised on a Cartesian grid. The variables, velocity and pressure, are defined on a staggered grid. The velocity components are computed on the faces of control volumes, the pressure is computed at the centre of the control volume. In this situation the boundary condition for pressure is not needed. For discretisation the finite differences approach is used. The time integration is done by an implicit second-order accurate scheme. To combine numerical efficiency with higher-order accuracy, we introduce the higher order terms as a "single-step" defect correction (Gullbrand et al., 2001). One can show that for smooth problems this procedure is adequate to maintain the theoretical accuracy of the high-order scheme. Hence, we obtain third-order accuracy for convective terms and fourth-order for other terms. At each time step the system of equations is solved by using a multi-grid solver. To reduce the number of cells, locally refined Cartesian grids are used in addition to uniform

global grids, as shown by Fuchs and Zhao (1984). The relaxation procedure involves the point-wise relaxation of the momentum equations coupled with point-wise smoothing of the continuity equation. Then both the velocity vector and pressure are corrected to satisfy the continuity equation while residuals of the momentum equations are not changed.

2.3. VB method

The VB method is based on the fact that the forces exerted on a body by the flow should equal the forces exerted on the flow by the body. The source terms representing the action of the body on the fluid are added to the momentum equation directly. The equations governing incompressible flow can then, in a nondimensional form, be written as

$$\frac{\partial u_i^*}{\partial x_i^*} = 0, \tag{12}$$

$$\frac{\partial u_i^*}{\partial t^*} + u_j^* \frac{\partial u_i^*}{\partial x_j^*} = -\frac{\partial p^*}{\partial x_i^*} + \frac{1}{\mathrm{Re}} \frac{\partial}{\partial x_j^*} \frac{\partial u_i^*}{\partial x_j^*} + \Phi_i, \tag{13}$$

where Φ_i are the forcing terms that make the flow satisfy the ith boundary condition. The magnitudes of these source terms are calculated based on the velocity defect, i.e. the deviation of the fluid velocity from the boundary velocity on the surface of the boundary. The forcing terms are updated through the iterative procedure of the flow solver. In short the method can be described by the following steps (a more detailed description is given by Revstedt (2004)):

(i) *Discretisation of the surface*: A two-dimensional grid is generated on the surface of the body, in such a way that the node distance is smaller but of the same order of magnitude as the mesh spacing of the flow solver.

(ii) *Determining the velocity defect*: The velocity of the boundary is calculated using a Gaussian weighted average of the flow velocities around the surface nodes,

$$u_i^f = \int_{\xi-2}^{\xi+2} \int_{\eta-2}^{\eta+2} \int_{\zeta-2}^{\zeta+2} u_i^* G_F \, \mathrm{d}\xi \, \mathrm{d}\eta \, \mathrm{d}\zeta, \tag{14}$$

where (ξ, η, ζ) is the boundary position normalised with the mesh spacing and G_F is a Gaussian distribution function

$$G_F = \frac{1}{(\sigma\sqrt{2\pi})^3} \, \mathrm{e}^{-(\xi^2+\eta^2+\zeta^2)/2\sigma^2}, \tag{15}$$

where σ is of the order of the computational grid size.

(iii) *Calculating the force contribution*: The force contributions on the surface nodes are calculated based on the difference between the calculated velocity on the boundary and the boundary condition

$$F_i^n = F_i^{n-1} + \Delta F_i^n, \quad \Delta F_i^n = \alpha \frac{u_i^f - u_i^b}{h^2}, \tag{16}$$

where h is the node distance of the computational grid.
With a desirable boundary velocity error accuracy one can calculate the new force distribution in the flow. Here u_i^b is the prescribed velocity of the boundary, n is an iteration number within one time step, α is a constant chosen to ensure both numerical stability as well as optimal numerical convergence.

(iv) *Distribution of the surface forces*: The surface forces are distributed using the same Gaussian function as is used for determining the boundary velocity. At the end of each time step after termination of the relaxations and calculation of the force acting on the cylinder, the equation of motion for an undamped cylinder is solved.

$$m^* \ddot{x}^* + k^* x^* = C_x. \tag{17}$$

The right-hand side of Eq. (17) is determined by integrating the source term in the x-direction momentum equation (13) over the whole volume Ω:

$$C_x = \frac{2D}{L} \int_\Omega \Phi_x \, \mathrm{d}\Omega. \tag{18}$$

Eq. (17) is solved by a fourth order Runge–Kutta method.

3. Computational set-up

The computational domains and the structure of the local refinements, used in the simulations, are shown schematically in Fig. 1. In the case of an unconfined cylinder the size of the computational domain is $12D$, $4D$ and $20D$ in the x-, y- and z-directions, respectively. For the confined flow the channel size is $6D$ and $10D$ in x- and z-directions, respectively, and equal to the cylinder length in the y-direction, i.e. $2D$, $4D$ or $8D$. The cylinder is in all cases positioned at a distance $4D$ from the inlet and is only allowed to move in the transversal direction (i.e. along the x-axis). In the inlet a uniform velocity profile ($u_z^* = 1, u_x^* = u_y^* = 0$) is specified and at the outlet a zero velocity gradient condition is applied. The outlet boundary condition is adjusted to satisfy the global mass conservation requirement. In the confined cases, no-slip boundary conditions are set on the outer walls of the domain. For the unconfined cylinder periodic conditions are used on the boundaries normal to the cylinder axis and free-slip conditions on the boundaries normal to the direction of motion of the cylinder. For other domain faces and the cylinder surface, a no-slip boundary condition is applied. The cylinder surface is defined using a VB method, as described above. The grid consists of several levels of local refinements, leading to a resolution $h = D/16$ close to the cylinder. The overall number of node points used is about one million. The temporal resolution is set to have a CFL number about 0.2.

4. Results

4.1. Sensitivity to blockage and grid resolution

The effects of blockage have been investigated for the stationary unconfined cylinder in order to find a suitable domain size. The distance between the boundaries parallel to the flow and the cylinder axis has been varied between 8 and 24 cylinder diameters and the grid resolution was set to $h = 0.0625$. The blockage ΔA is defined as the ratio between the projected area of the cylinder normal to the flow direction and the inlet area. Hence, the given variation of domain height corresponds to blockages between 12.5% and 4.7%. Fig. 2 shows the average drag coefficient (C_D) and the nondimensional shedding frequency (St) for both Reynolds numbers. As can be seen, the influence of domain height on

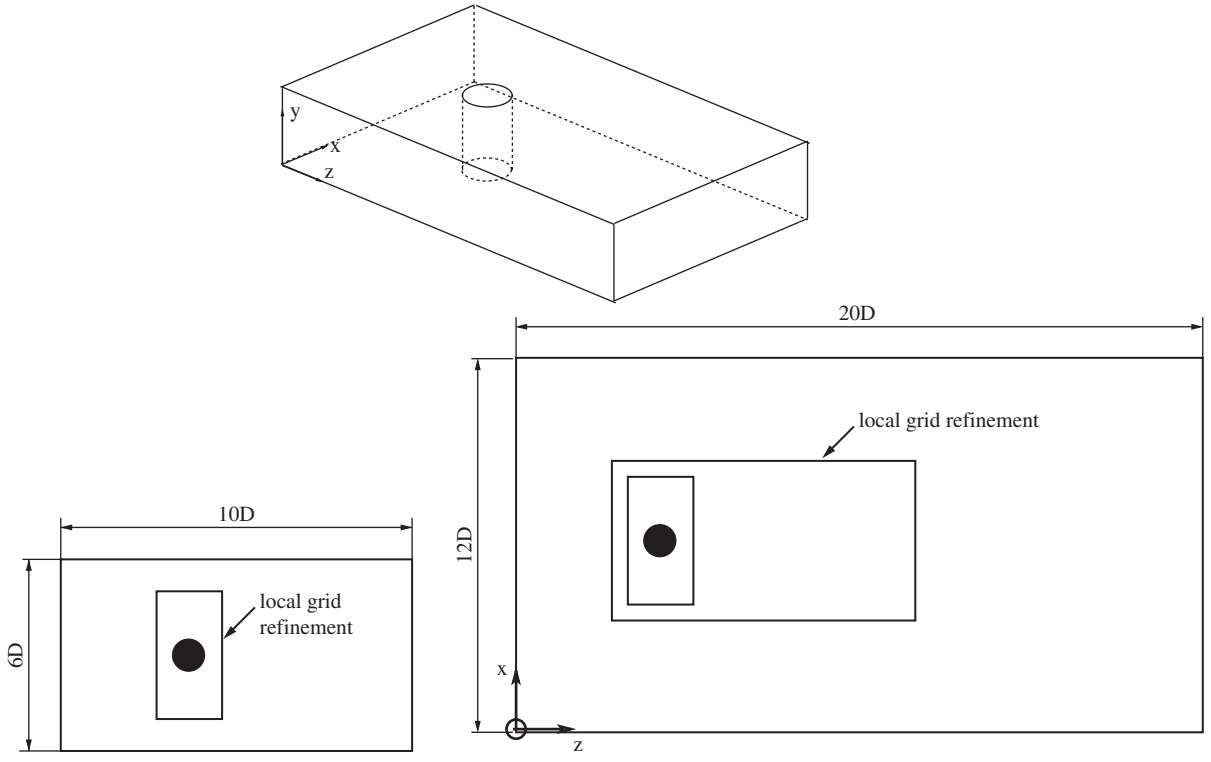

Fig. 1. Geometry, coordinate system and location of grid refinements for confined (left) and unconfined (right) cylinders.

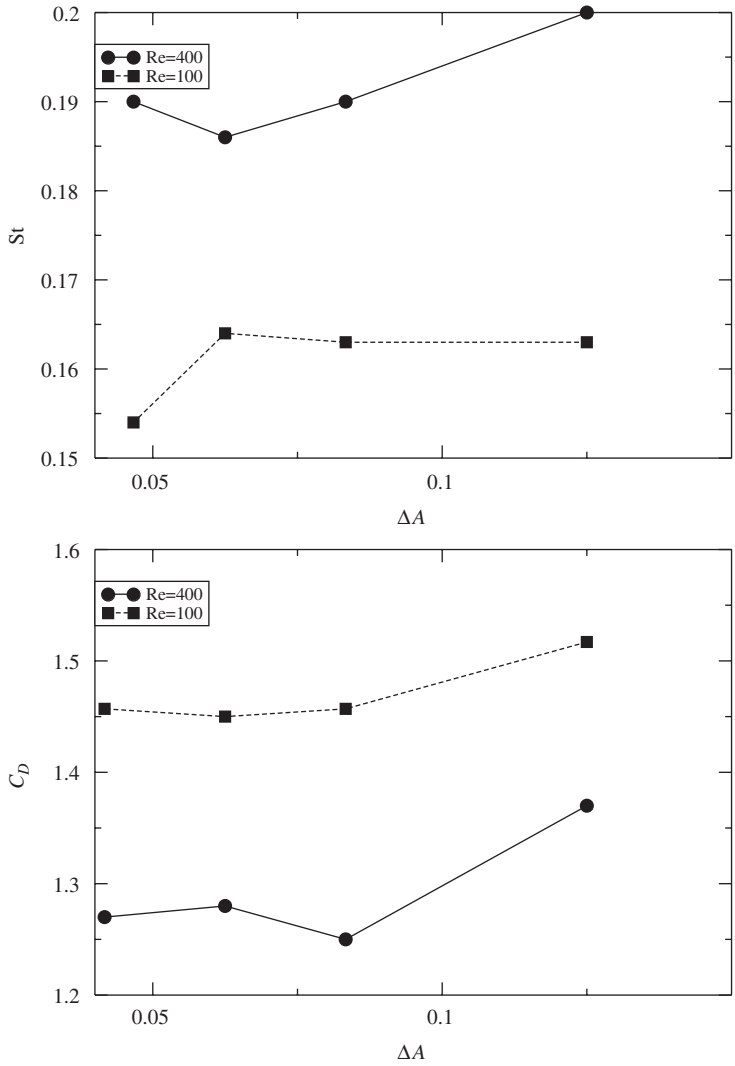

Fig. 2. Mean drag coefficient and shedding frequency as a function of the area blockage, ΔA.

these variables is minor already at $\Delta A = 8.3\%$. The study of the influence of grid resolution was performed for the case of 8.3% blockage. We consider the average drag coefficient and the nondimensional shedding frequency at three levels of grid resolution ($h = D/8$, $D/16$ and $D/32$). The results are presented in Fig. 3. Considering C_D, the change when going from $h = D/16$ to $D/32$ is less than 2%. For the frequency the variation is somewhat higher (around 5%) for $\mathrm{Re} = 200$. However, in the following we have chosen to use a domain size of $12D \times 4D \times 20D$, i.e. a blockage of 8.3% for the unconfined cylinder and a grid resolution $h = D/16$ for all cases.

4.2. Boundary errors

The source terms Φ should act so that the boundary conditions (u_i^b) are satisfied on the nodes on the VB. As was noted by Revstedt and Fuchs (2001), one will have an error in the boundary velocity (u_i^f) which is dependent on the method with which one determines the velocity on the boundary and the method for distributing the source terms back to the flow field. The method used here (Eqs. (14)–(16)) is first-order accurate. Revstedt (2004) has shown that, by employing a higher-order extrapolation method to determine the boundary velocity and by limiting the distribution of source terms to the interior of the object, one can achieve second-order accuracy. However, that approach has been

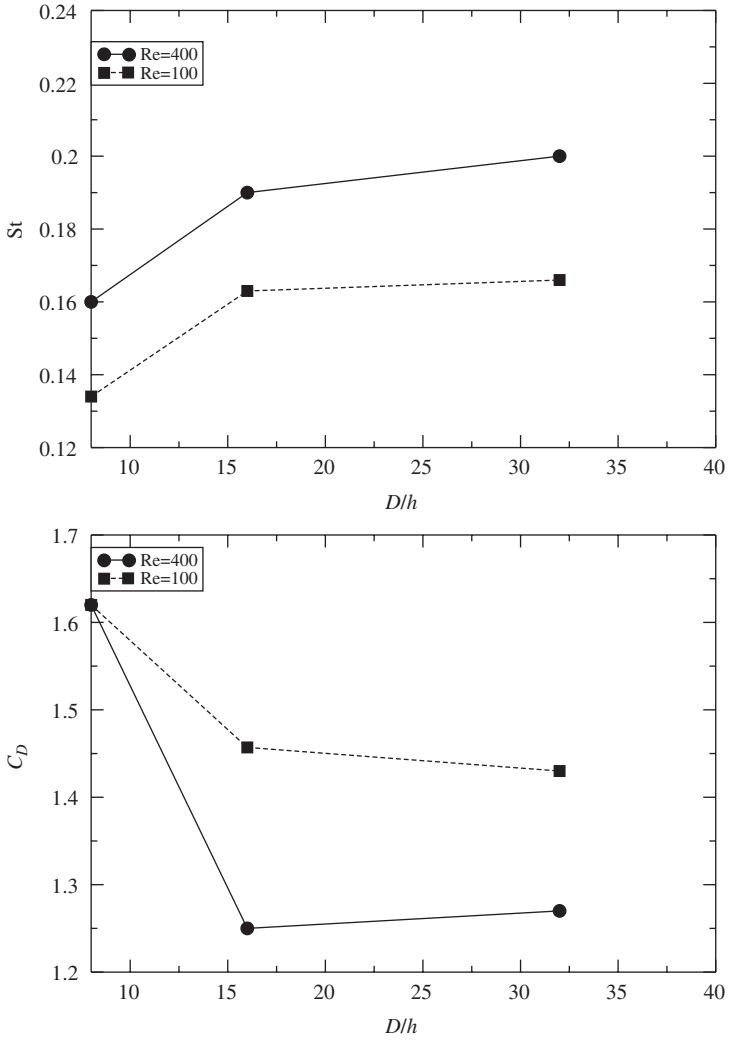

Fig. 3. Mean drag coefficient and shedding frequency as a function of the number of cells over one cylinder diameter, D/h.

shown to be unstable for moving objects. To determine how well the boundary conditions on the cylinder surface are fulfilled we consider the L_2-norm of the difference between the fluid velocity and the boundary condition. Hence, the error is defined as

$$\varepsilon_i^{L_2} = \sqrt{\frac{1}{N}\sum_{n=1}^{N}(u_i^f - u_i^b)^2}, \tag{19}$$

where N is the total number of nodes on the VB.

Fig. 4 shows the time average of the L_2-norm of the errors in boundary velocity in the x- and z-directions, $\overline{\varepsilon_i^{L_2}}$, as a function of amplitude for the short confined cylinder. The errors increase somewhat with increasing amplitude, which of course is related to the increasing speed of the cylinder. However, the errors are below 1.5% of the channel bulk velocity.

The vortex-induced vibration of a single circular cylinder has been studied in the situation when the flow was confined by a rectangular channel. Simulating the flow past a stationary circular cylinder in this configuration, we found that at $\mathrm{Re} = 400$ the lift fluctuation has very periodical character and the wake is laminar.

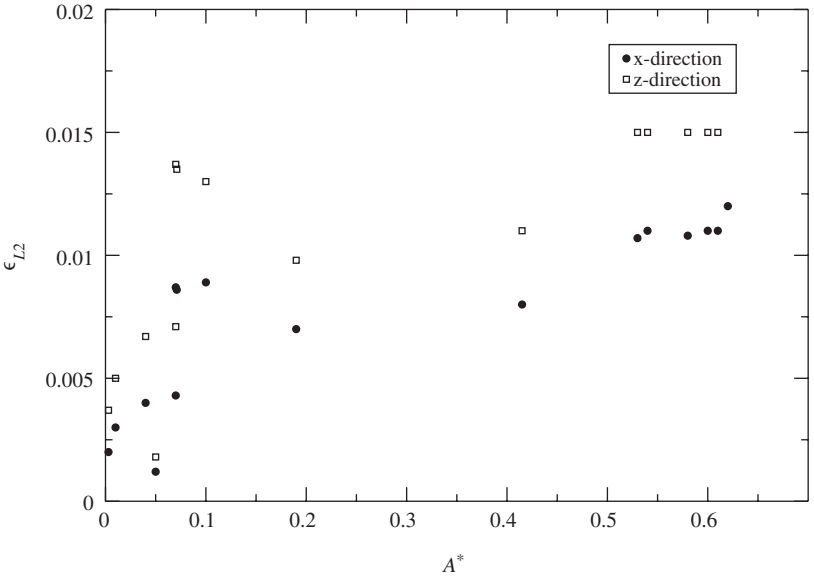

Fig. 4. L_2-norm of the error in boundary velocities in the main flow and cross-stream directions.

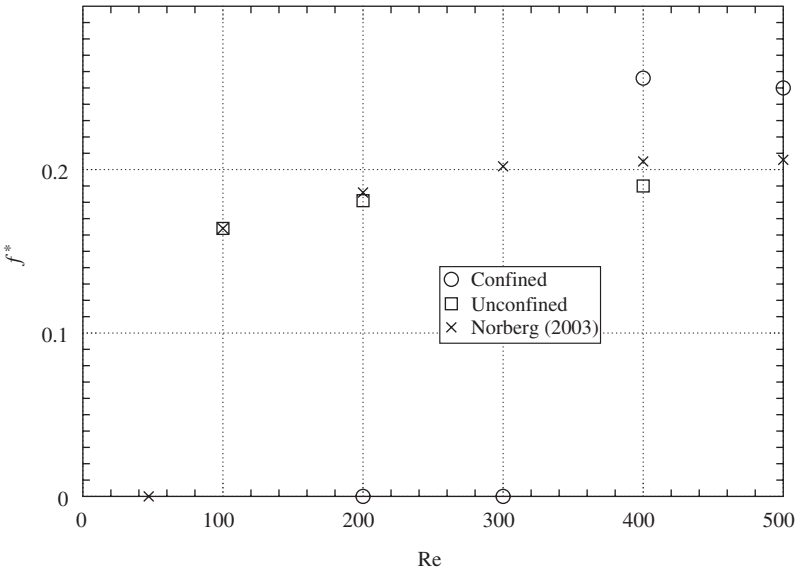

Fig. 5. Strouhal number of the vortex shedding as a function of Reynolds number for confined ($L = 2D$) and free cylinders, compared to empirical data.

4.3. Stationary confined cylinder

We have studied flow around stationary cylinders, confined as well as unconfined, in the range $100 \leqslant \mathrm{Re} \leqslant 400$. Fig. 5 shows the frequency of vortex shedding for both confined and unconfined flow around cylinders compared to the experimental results by Norberg (2003). In this particular case the length of the confined cylinder is $L = 2D$. One may conclude that major effects of confinement on the flow are the higher shedding frequency and the later onset of the time dependent wake. Hence, the confinement seems to have a damping effect on the flow. This is further illustrated in Fig. 6, which shows the instantaneous velocity fields for confined and unconfined cylinders at $\mathrm{Re} = 400$. The iso-contours are a λ_2-visualisation of the wake vortices. The λ_2-method, introduced by Jeong and Hussain (1995), is a method for

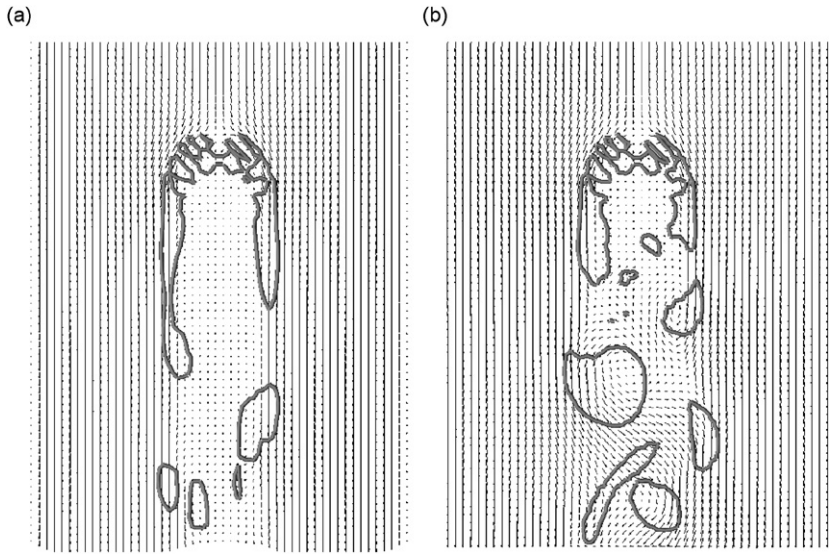

Fig. 6. Snapshot of the velocity fields and λ_2 visualisation of the wake vortices at mid-span for: (a) a confined ($L = 2D$) and (b) an unconfined cylinder at $\mathrm{Re} = 400$.

identifying vortices. By studying the eigenvalues of the tensor created by the sum of the squares of the symmetric and antisymmetric parts of the velocity gradient tensor one can identify local pressure minima caused by a vortex core as locations where two eigenvalues are negative. Hence, plotting iso-contours of negative values of the middle eigenvalue (λ_2), one can visualise vortices. One can here clearly see that, in the confined case, the wake is narrower, the vortices are stretched along the main flow direction and the vortex shedding occurs further downstream than in the unconfined case. Furthermore, the confinement effect also results in higher mean drag and much lower value of lift fluctuation compared to the unconfined flow. For the short ($L = 2D$) confined cylinder at $\mathrm{Re} = 400$ we get the following values of mean drag, lift fluctuations and shedding frequency $f_0^* = f_0 U/D : C_D = 1.47$, $C_{L\mathrm{rms}} = 0.011$ and $f_0^* = 0.256$. Corresponding values for an unconfined cylinder are: $C_D = 1.27$, $C_{L\mathrm{rms}} = 0.27$ and $f_0^* = 0.195$. Considering Fig. 5, $\mathrm{Re} = 400$ is the lowest possible value that can be used in the confined cases.

4.4. Undamped vortex-induced vibration of cylinder

In all the simulations in the present work we have chosen to disregard damping, i.e. $b^* = 0$. This simplifies numerical analysis of the problem without losing the main point of the study, which is to investigate the influence of confinement on the cylinder motion and synchronisation. The study is conducted using a mass ratio $m^* = \pi$. The cylinder length, and consequently also the distance between the side walls is varied. The results obtained are compared to those for an unconfined cylinder. Mainly, the results will be presented as a function of the effective elasticity, as defined by Shiels et al. (2001):

$$k_{\mathrm{eff}}^* = k^* - 4\pi^2 (f^*)^2 m^*. \tag{20}$$

In the case of regular cylinder response, the cylinder motion can be described by this single parameter. Having $k_{\mathrm{eff}}^* = 0$ corresponds to the resonance situation, $f^* = f_N^*$. Following the classical theory of lock-in one would expect to observe the maximal oscillation amplitude at $k_{\mathrm{eff}}^* = 0$. However, at low mass ratios the influence of the added mass on the natural frequency cannot be neglected. Therefore, we find, in agreement with recent experimental and numerical studies, a range of k_{eff}^* where the maximal amplitude of cylinder oscillation has a relatively high value. It should be noted that the reduced velocity decreases with increasing k_{eff}^*, as can be seen in Fig. 7.

4.4.1. Unconfined cylinder

Fig. 8, shows the amplitude A^*, the cylinder oscillation frequency f^* and drag coefficient as functions of the effective elasticity for an unconfined cylinder at $\mathrm{Re} = 100$. For this case the high amplitude range is observed, implying a very steep increase in the amplitude at $k_{\mathrm{eff}}^* = 0$.The range of k_{eff}^*, where amplitude has its maximum high value, is approximately between -0.13 and 0.64. The frequency also undergoes dramatic chances at k_{eff}^* close to 0, first rapidly

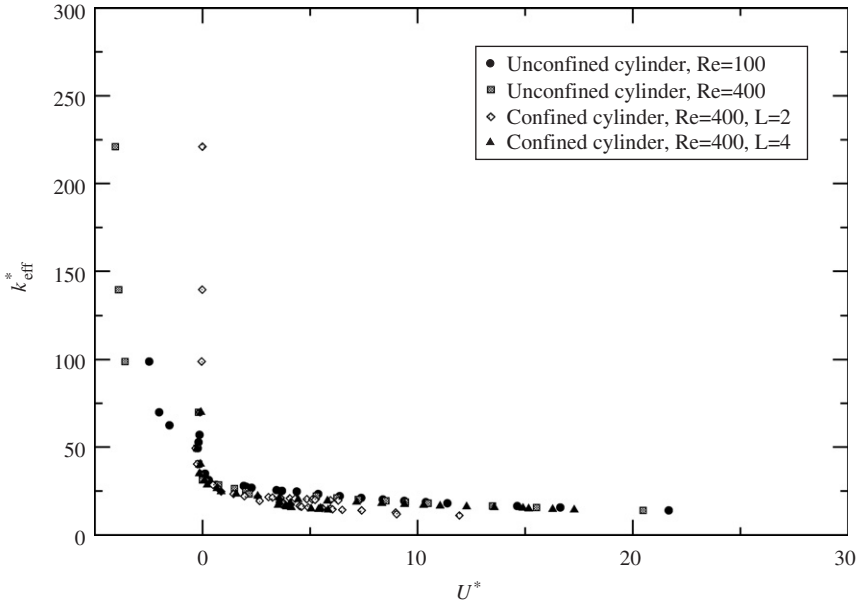

Fig. 7. Reduced velocity as a function of effective elasticity for the cases considered.

decreasing and then increasing. Beyond $k^*_{\text{eff}} = 0.64$ the amplitude rapidly decreases, and the vibrational frequency tends to a constant value close to the shedding frequency of a stationary cylinder. Also, note that the drag coefficient exhibits a similar behaviour as the amplitude. Our results show good agreement with those obtained by Shiels et al. (2001), except that our simulations predict a faster decay of the amplitude and somewhat higher mean drag coefficient. What happens at k^*_{eff} close to zero is more clear if one plots the frequency and amplitude against the natural frequency, Fig. 9. At low f^*_N the cylinder vibrates with a low amplitude and a frequency governed by the vortex shedding. As k^* is increased the frequency drops and locks-in to the natural frequency of the system. The two solid vertical lines in Fig. 9 indicate the boundaries of the lock-in range for $\text{Re} = 100$ and the dashed lines the range for 400. Hence, the lock-in range becomes somewhat wider with increasing Reynolds number. In this range the vibrational frequency is very close to the natural one and the amplitude is gradually increased with increasing f^*_N (which corresponds to decreasing reduced velocity). Beyond the lock-in range we again observe the steep decay in amplitude and that the frequency approaches a constant value, which is similar to the shedding frequency for a stationary cylinder. Comparing the amplitudes at $\text{Re} = 100$ and 400, one observes no significant changes with Reynolds number. Considering the force coefficient, the mean drag and drag fluctuations decrease with increasing Reynolds number, however, the lift fluctuations seem unaffected by the change in Reynolds number (Fig. 10). An indication to what causes the significant difference in drag fluctuations can be found by comparing the wake structures. Fig. 11 shows λ_2 visualisations of the wake vortices for $\text{Re} = 100$ and 400 at $k^* = 5$. For $\text{Re} = 100$ the wake is essentially two-dimensional and very regular. However, increasing the Reynolds number a longitudinal mode of fluctuations strongly affects the vortices (probably mode B vortex shedding), causing the wake to be highly three-dimensional.

4.4.2. *Confined cylinder*

Fig. 12 depicts the amplitude of cylinder motion as a function of the effective elasticity. For the confined cases we find no difference in amplitude in the lock-in range compared to the unconfined cases. However, for higher values of k^*_{eff}, the amplitude is somewhat lower in the confined cases. Furthermore, the width of the lock-in range, in terms of k^*_{eff}, seems to be independent of the confinement effect.

However, the major difference is in the frequency of motion. Both unconfined cases show similar behaviour, i.e. a rapid change in frequency locking on to the natural frequency at the beginning of the synchronisation range and thereafter a decay towards a constant value. The confined cases also show qualitatively similar behaviour as the unconfined cases in the synchronisation range. Before and after this range the confined cases differ significantly from the unconfined cases, which can be observed in Fig. 13. Taking a closer look at this phenomenon, we turn to Fig. 14 which shows the vibrational frequency as a function of the natural frequency of the structure (f^*_N). In the post-synchronisation range, the frequency of the very short cylinder ($L = 2D$) increases monotonically with increasing spring

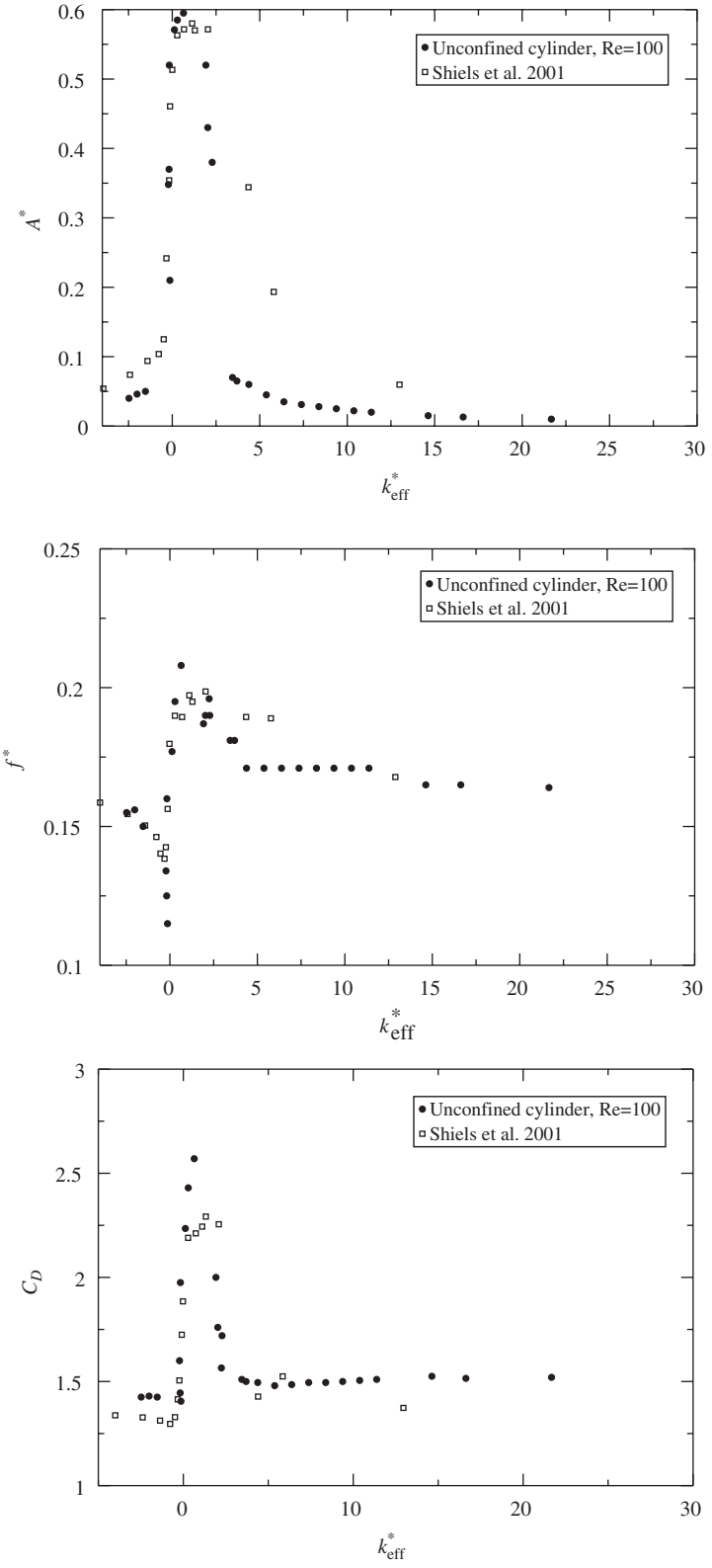

Fig. 8. Amplitude and frequency of the cylinder motion, and average drag coefficient for an unconfined cylinder at $\mathrm{Re} = 100$ compared to the results by Shiels et al. (2001).

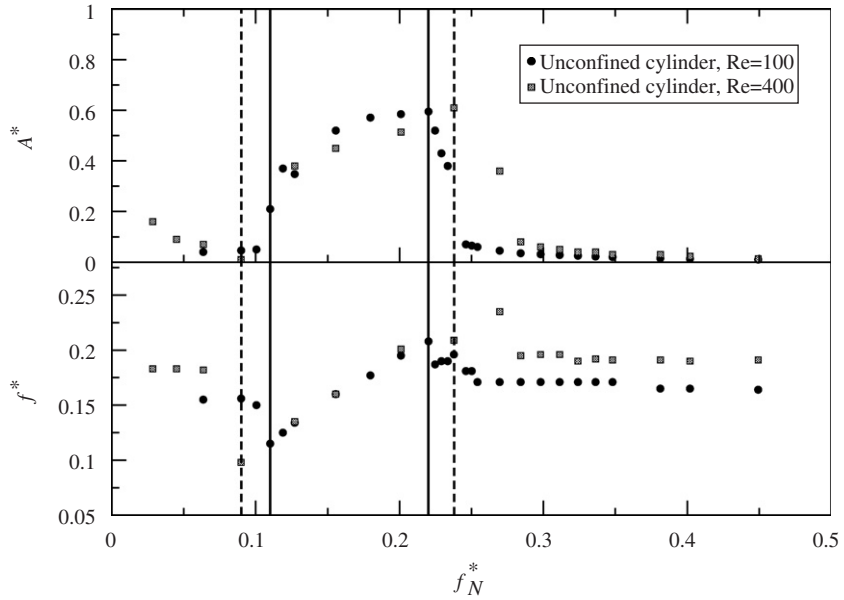

Fig. 9. Amplitude and frequency of the cylinder motion as a function of the natural frequency.

stiffness (k^*). In the case of a longer cylinder ($L = 4D$) the curves bifurcate, with one branch going towards a constant value of vibration frequency and the other increasing monotonically. In the synchronisation range (starting at $f_N^* \approx 0.1$ for the unconfined cases) $f^* \approx f_N^*$, hence the slope of the solid line in Fig. 14 is very close to unity. Above the synchronisation range the frequency drops off towards a constant value. However, for the short confined cylinder this decrease is stopped at $f_N^* \approx 0.325$, corresponding to an elasticity coefficient, $k^* = 12.75$, and again starts to increase linearly, but with $f^* \approx 0.85 f_N^*$. This value of the vibrating frequency is very close to the natural frequency in a still fluid. Accounting for the added mass the natural frequency can be written as

$$f_A^* = \frac{1}{2\pi}\sqrt{\frac{k^*}{m^* + m_a^*}}, \tag{21}$$

where m_a^* is the nondimensional added mass. Using potential theory the added mass equals the mass of the displaced fluid, i.e. $m_a^* = 1$. With $m^* = \pi$ the ratio between the natural frequencies in vacuum and in still fluid is

$$\frac{f_A^*}{f_N^*} = \sqrt{\frac{\pi}{\pi + 1}} \approx 0.87. \tag{22}$$

Hence, for the very short cylinder ($L = 2D$) the motion is governed by the natural frequency, even outside the synchronisation range. It should be noted that this response is also found for the unconfined cylinders, however, only in a very small range of k^*. When doubling the length of the cylinder one will have both modes present, the one related to the structural frequency and the one related to the vortex shedding frequency, with approximately equal strength. We have not been able to find any pre-synchronisation range (high U^*) for the confined cylinders in the sense that the motion should be governed by the shedding frequency. As can be seen in Fig. 14, the motion is locked on to the natural frequency even for very low values of spring stiffness.

Fig. 15 shows the Fourier transform of the time history of the cylinder position for lengths $L = 2D$, $4D$ and $8D$ at $k^* = 17$. The figure shows that both frequencies are present in all three cases. At $L = 2D$ the higher frequency dominates and as the cylinder length is increased the lower frequency mode, which is related to the vortex shedding, starts to dominate. Hence, for long confined cylinders the vibrational behaviour tends to the one observed for unconfined cylinders, as would be expected. The value of the shedding frequency though, seems to be influenced only by the blockage effect, i.e. the distance between the walls in the transversal direction. Further explanation to this phenomenon can be found by considering the wake structure at different wall distances. Fig. 16 shows the λ_2 visualisations of the instantaneous vortex structures in the wake at $L = 2D$, $4D$ and $8D$. As can be seen the wake structures are highly three-dimensional. At $L = 2D$ the vortices gets a "horse-shoe" form almost immediately after

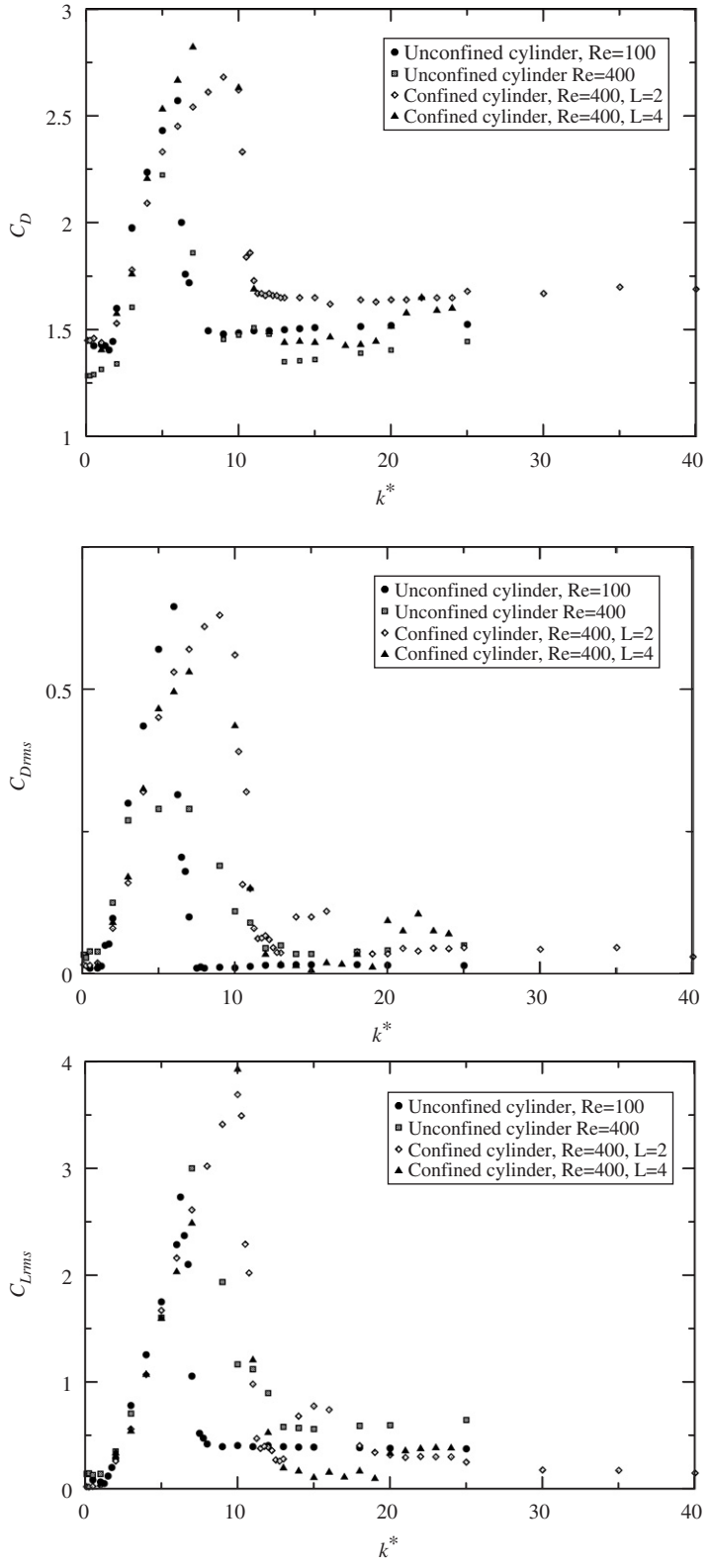

Fig. 10. Mean drag coefficient and rms. of drag and lift coefficients fluctuations as a function of the elasticity.

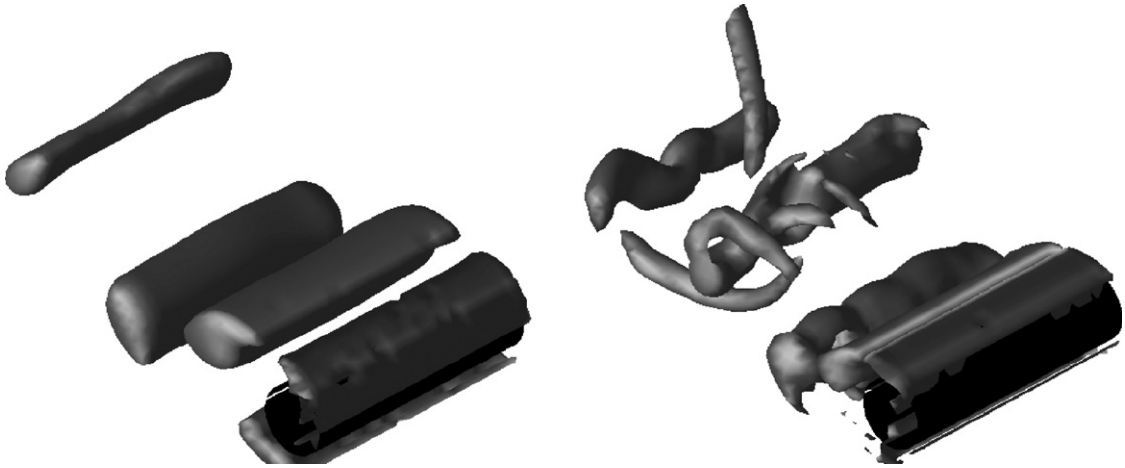

Fig. 11. λ_2 visualisation of the wake structure of the unconfined cases at $k^* = 5$ for Re = 100 (left) and 400 (right).

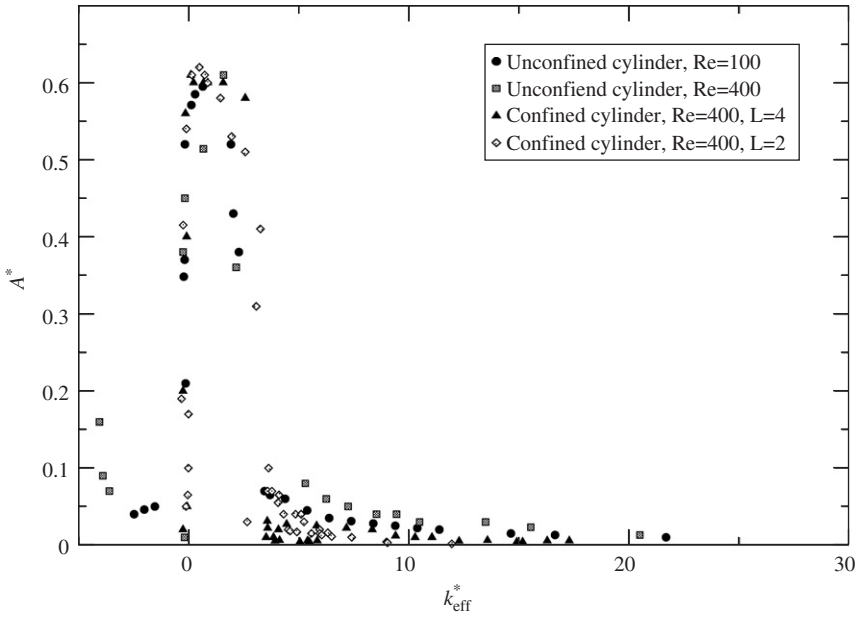

Fig. 12. The amplitude of the cylinder motion as a function of the effective elasticity.

shedding. This is of course due to the velocity variations in the wall-normal direction. Increasing the length to $L = 4D$ this effect is less pronounced but still clearly visible, and finally at $L = 8D$ we obtain a wake structure with very limited wall effects and strongly affected by the second mode of vortex shedding, i.e. very similar to the unconfined case (Fig. 11). Fig. 17 depicts the time histories of cylinder motion at several values of spring stiffness in the range $7 \leqslant k^* \leqslant 30$ for the short ($L = 2D$) confined cylinder. In the synchronisation range ($k^* = 7 \Leftrightarrow U^* \approx 0.670$) one observes a very regular, high amplitude response which persists until the end of this range ($k^* = 10 \Leftrightarrow U^* \approx 0.560$). Just beyond the synchronisation range ($k^* = 12 \Leftrightarrow U^* \approx 0.512$) the motion has a low frequency modulation. Further increasing the stiffness, the response again becomes more regular with a temporary increase in amplitude around $k^* = 15$ ($U^* \approx 0.458$), and thereafter a decreasing amplitude as the stiffness is increased ($k^* = 30 \Leftrightarrow U^* \approx 0.323$).

The forces acting on the confined cylinder are depicted in Fig. 10. As for the unconfined cases, a large increase in mean drag as well as drag and lift fluctuations is observed as the synchronisation range is entered. This is expected and follows well the increase in vibration amplitude. Comparing the confined and unconfined cylinders at Re = 400 one can see that in the synchronisation range the mean drag and the drag fluctuations are larger in the confined case. However, the differences in lift fluctuations are much smaller.

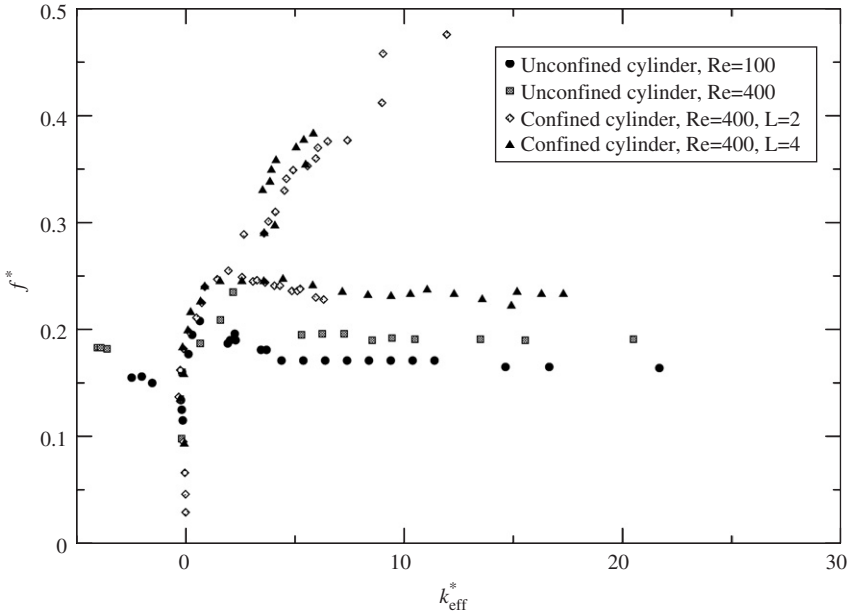

Fig. 13. The frequency of the cylinder motion as a function of the effective elasticity.

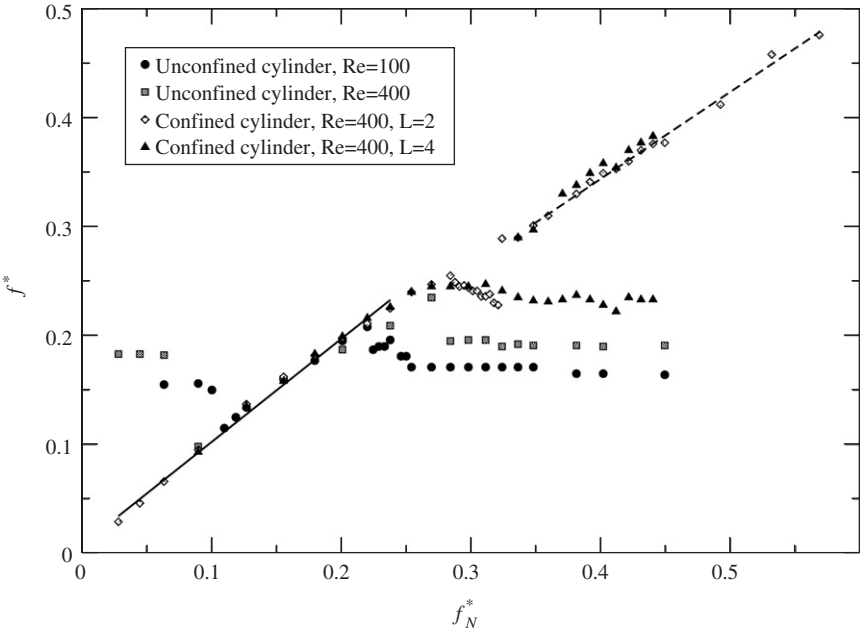

Fig. 14. Vibrational frequency of the cylinder as a function of the natural frequency.

5. Summary and conclusions

A VB method has been applied to the problem of flow-induced motion of an elastically mounted cylinder at moderate Reynolds number. The results for an unconfined cylinder at $\mathrm{Re} = 100$ show good agreement concerning vibrational amplitude, frequency and drag force and with the two-dimensional simulation data by Shiels et al. (2001).

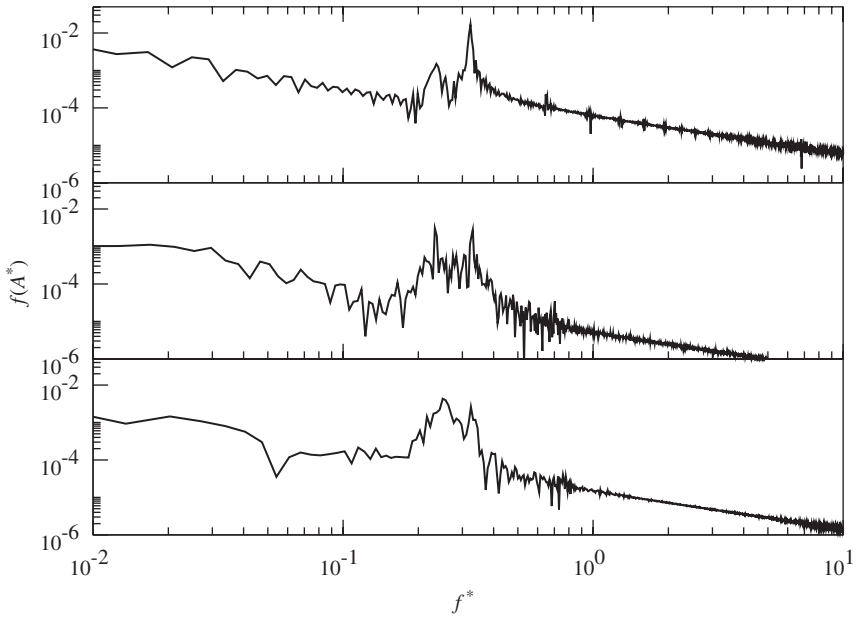

Fig. 15. The Fourier transform of the amplitude ($\mathcal{F}(A^*)$) for the confined cylinder at $k^* = 17$ with $L = 2D$ (top), $L = 4D$ (middle) and $L = 8D$ (bottom).

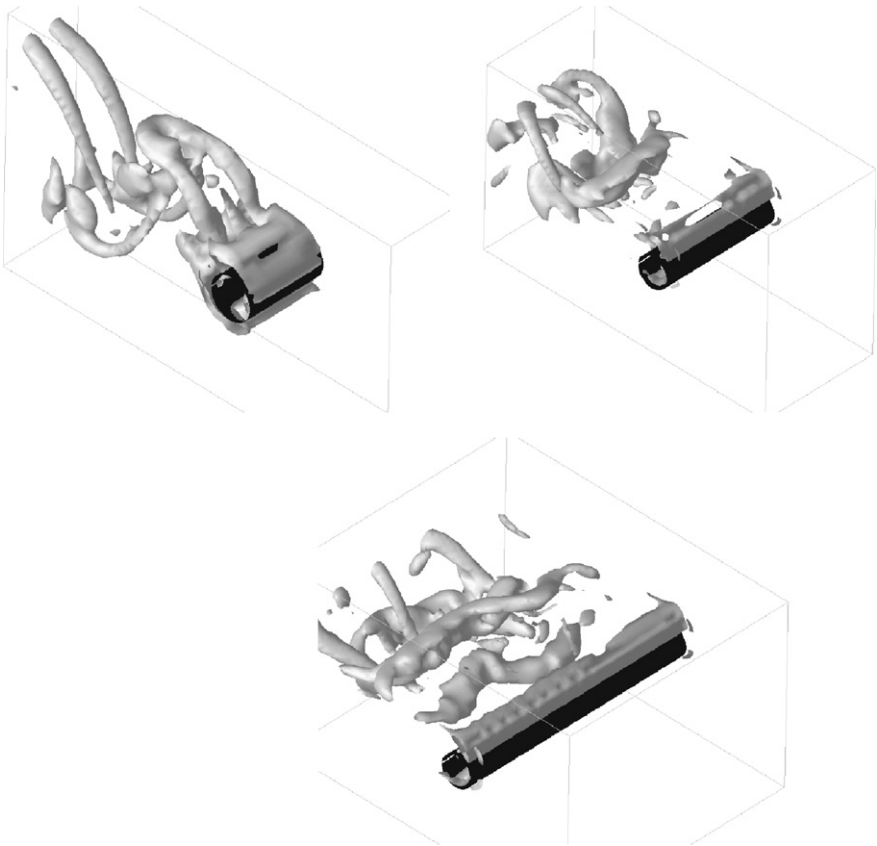

Fig. 16. λ_2 visualisation of the wake structure of the confined cases at $k^* = 17$ for $L = 2D$ (top left), 4D (top right) and $8D$ (bottom).

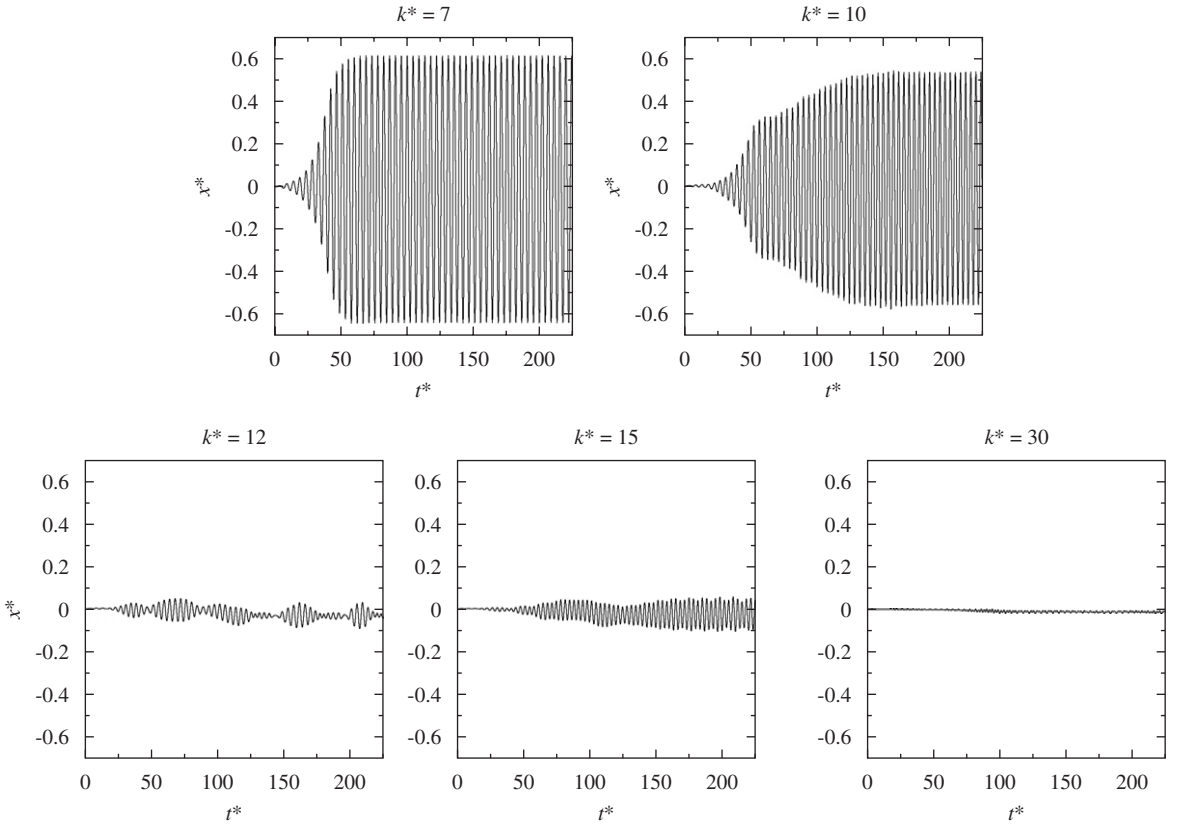

Fig. 17. Time history of the amplitude at several values of elasticity for a confined cylinder with $L = 2D$.

Comparing unconfined and confined flow around cylinders one can conclude the following.

- For stationary cylinders one obtains higher mean drag, higher shedding frequency and lower lift fluctuations in the confined case. This is an effect of the blockage, i.e. the position of the walls in the transversal direction.
- For moving cylinders at equal Reynolds numbers, the mean drag coefficient and the drag coefficient fluctuations are lower in the unconfined case. In the confined cases the drag, both mean and fluctuating, is much closer to the one obtained for an unconfined cylinder at $\mathrm{Re} = 100$. This is probably an effect of the presence of the walls suppressing the longitudinal modes of vortex shedding, hence creating a more structured wake. However, it should be noted that the effect on lift fluctuations is much smaller, and that the amplitude of motion in the synchronisation range is unaffected by both confinement and a change in Reynolds number.
- The upper boundary of the synchronisation range is mainly a function of Reynolds number, i.e. the range extends to larger values of elasticity coefficient as the Reynolds number is increased. However, in the confined cases no lower boundary was found. The cylinder motion was locked on to the natural frequency of the system even for very low values of elasticity coefficient.
- For a very short cylinder $L = 2D$, the motion is strongly influenced by the elasticity coefficient, even beyond the synchronisation range. Here the cylinder is moving with a low amplitude and a frequency which is about 85% of the natural frequency in vacuum. This value is found to be very close to the natural frequency in still fluid. This range is also found for unconfined cylinders, however, in a much narrower range of elasticity, where it would correspond to an initial branch response [e.g. Khalak and Williamson (1996)]. As the cylinder length is increased, the mode related to the vortex shedding starts to dominate leading to a frequency of motion independent of the elasticity coefficient.

Acknowledgements

This work was financially supported by the Swedish National Energy Administration (STEM), Grant No. 12126-c. The computational resources provided by the Swedish National Infrastructure for Computing (SNIC) and the Centre for Scientific and Technical Computing at Lund University (LUNARC) is also gratefully acknowledged.

References

Bearman, P., 1984. Vortex shedding from oscillating bluff bodies. Annual Review of Fluid Mechanics 16, 195–222.

Brika, D., Laneville, A., 1993. Vortex-induced vibrations of a long flexible cylinder. Journal of Fluid Mechanics 250, 481–508.

Esmaeeli, A., Tryggvason, G., 1998. Direct numerical simulations of bubbly flows: part 1: Low Reynolds number arrays. Journal of Fluid Mechanics 377, 313–345.

Feng, C., 1968. The measurements of vortex-induced effects in flow past stationary and oscillating circular and D-section cylinders. Ph.D. Thesis, University of British Columbia, Vancouver, BC, Canada.

Fuchs, L., Zhao, H.-S., 1984. Solution of three-dimensional viscous incompressible flows by a multi-grid method. International Journal of Numerical Methods in Fluids 4, 539–555.

Govardhan, R., Williamson, C., 2000. Models of vortex formation and frequency response of a freely-vibrating cylinder. Journal of Fluid Mechanics 420, 85–130.

Govardhan, R., Williamson, C., 2001. Mean and fluctuating velocity fields in the wake of a freely-vibrating cylinder. Journal of Fluids and Structures 15, 489–501.

Gullbrand, J., Bai, X.-S., Fuchs, L., 2001. High-order cartesian grid method for calculation of incompressible turbulent flow. International Journal of Numerical Methods in Fluids 36, 539–555.

Jeong, J., Hussain, F., 1995. On the identification of a vortex. Journal of Fluid Mechanics 285, 69–94.

Khalak, A., Williamson, C., 1996. Dynamics of a hydroelastic cylinder with very low mass damping. Journal of Fluids and Structures 10, 455–472.

Khalak, A., Williamson, C., 1999. Motions, forces and mode transitions in vortex-induced vibrations at low mass-damping. Journal of Fluids and Structures 13, 813–851.

Koopmann, G., 1967. The vortex wakes of vibrating cylinders at low Reynolds number. Journal of Fluid Mechanics 28, 501–512.

Norberg, C., 2003. Fluctuating lift on a circular cylinder: review and new measurements. Journal of Fluids and Structures 17, 57–96.

Parkinson, G., 1989. Phenomena and modelling of flow-induced vibrations of bluff bodies. Progress in Aerospace Science 26, 169–224.

Peskin, C., 1977. Numerical analysis of blood flow in the heart. Journal of Computational Physics 25, 220–252.

Revstedt, J., 2004. A virtual boundary method with improved accuracy and computational efficiency. International Journal of Numerical Methods in Fluids 45, 775–795.

Revstedt, J., Fuchs, L., 2001. Handling complex boundaries on a Cartesian grid using surface singularities. International Journal of Numerical Methods in Fluids 35, 125–150.

Sarpkaya, T., 1979. Vortex-induced oscillations—a selective review. Journal of Applied Mechanics 46, 241–258.

Shiels, D., Leonard, A., Roshko, A., 2001. Flow-induced vibration of a circular cylinder at limiting structural parameters. Journal of Fluids and Structures 15, 3–21.

Shyy, W., Udaykumar, H., Choi, D., 1998. Structured moving grid and geometric conservation laws for fluid flow computation. Numerical Heat Transfer, Part A 34, 369–397.